Correlation analysis of strongly fluctuating atomic volumes, charges, and stresses in body-centered cubic refractory high-entropy alloys

Ishibashi, Shoji; Ikeda, Yuji; Körmann, Fritz; Grabowski, Blazej; Neugebauer, Jörg

DOI
10.1103/PhysRevMaterials.4.023608

Publication date
2020

Document Version
Final published version

Published in
Physical Review Materials

Correlation analysis of strongly fluctuating atomic volumes, charges, and stresses in body-centered cubic refractory high-entropy alloys

Shoji Ishibashi,[1,2,3,*] Yuji Ikeda,[1,4] Fritz Körmann,[1,5] Blazej Grabowski,[4] and Jörg Neugebauer[1]

[1]*Computational Materials Design, Max-Planck-Institut für Eisenforschung GmbH, D-40237 Düsseldorf, Germany*

[2]*Research Center for Computational Design of Advanced Functional Materials (CD-FMat), National Institute of Advanced Industrial Science and Technology (AIST), Tsukuba, Ibaraki 305-8568, Japan*

[3]*Center for Materials Research by Information Integration (CMI^2), Research and Services Division of Materials Data and Integrated System (MaDIS), National Institute for Materials Science (NIMS), Tsukuba, Ibaraki 305-0047, Japan*

[4]*Institute of Materials Science, University of Stuttgart, Pfaffenwaldring 55, D-70569 Stuttgart, Germany*

[5]*Materials Science and Engineering, Delft University of Technology, 2628 CD, Delft, The Netherlands*

(Received 5 August 2019; revised manuscript received 20 December 2019; accepted 2 January 2020; published 27 February 2020; corrected 3 March 2020)

Local lattice distortions in a series of body-centered cubic alloys, including refractory high-entropy alloys, are investigated by means of atomic volumes, atomic charges, and atomic stresses defined by the Bader charge analysis based on first-principles calculations. Analyzing the extensive data sets, we find large distributions of these atomic properties for each element in each alloy, indicating a large impact of the varying local chemical environments. We show that these local-environment effects can be well understood and captured already by the first and the second nearest neighbor shells. Based on this insight, we employ linear regression models up to the second nearest neighbor shell to accurately predict these atomic properties. Finally, we find that the elementwise-averaged values of the atomic properties correlate linearly with the averaged valence-electron concentration of the considered alloys.

DOI: 10.1103/PhysRevMaterials.4.023608

I. INTRODUCTION

Refractory high-entropy alloys (HEAs), composed mainly of refractory elements from groups 4, 5, and 6 in the Periodic Table, have attracted interest due to their excellent high-temperature mechanical properties [1]. For example, the first reported refractory HEAs, NbMoTaW and VNbMoTaW, show higher yield strengths than typical Ni-based superalloys in a wide temperature range [2,3]. Another appealing example is TiZrNbHfTa, which has higher compressive ductility than NbMoTaW and VNbMoTaW at a significantly lower density, while maintaining an acceptable yield strength [4]. In general refractory HEAs reveal much larger yield strengths and Vickers hardnesses than the constituent elements [4–7], which is an indication of the extraordinary solid solution strengthening in HEAs.

While models of solid solution strengthening for conventional alloys were proposed many decades ago [8–10], theories for HEAs were reported only recently. The development has been mainly focused on an extension of the traditional Labusch model [10] to multicomponent alloys [11,12] or an application of the average effective-medium approach [13–15]. In any such development, quantities such as lattice misfit and effective atomic volume play an important role, which implies that local lattice distortions constitute a good descriptor to estimate the magnitude of solid solution strengthening in HEAs.

Local lattice distortions in disordered alloys have been analyzed in various ways, e.g., via atomic size mismatch of the different constituents [16]. For CrMnFeCoNi-based face-centered cubic (fcc) HEAs, the root-mean-square (RMS) atomic displacements from the ideal lattice sites were found by atomistic simulations to correlate well with the normalized (by the shear modulus) yield strength [17]. A correlation between atomic size misfit parameters and atomic displacements of HEAs was also discussed in several works [18,19]. In other works atomic volumes were investigated by means of Voronoi tessellation [20,21]. The concept of atomic-level pressure has been employed to analyze local lattice distortions and solid solution strengthening in HEAs [22,23]. Such concepts have been successfully employed to design new alloys with higher strength than available before [21,23].

The majority of the investigations of local lattice distortions has so far focused on fcc based HEAs. Similar studies for bcc alloys—which are generally more prone to distortions—are lacking, in particular when it comes to an explanation in terms of the electronic structure. In the present study we remedy this deficiency and analyze atomic volumes, atomic charges, atomic stresses, and mutual correlations for an extended set of 15 body-centered cubic (bcc) refractory alloys including refractory HEAs utilizing first-principles calculations. In particular, the atomic volumes, atomic charges, and atomic stresses are calculated based on the Bader charge

*shoji.ishibashi@aist.go.jp

analysis [24,25], and the relation to the local chemical environment is established.

II. COMPUTATIONAL DETAILS

We consider in total 15 equiatomic bcc alloys from binaries up to quinaries, namely VW, MoTa [26], VNbW, VTaW, ZrNbHf [27], NbMoTa, TiVNbTa [6], VNbMoTa [5], VNbTaW [6], NbMoTaW [2,3], TiVNbMoTa [7], TiVNbTaW [6], TiZrNbHfTa [4], TiZrMoHfTa [28], and VNbMoTaW [2,3]. All these alloys are made of nonmagnetic refractory elements of the groups 4, 5, and 6, namely Ti, V, Zr, Nb, Mo, Hf, Ta, and W. The selection of the alloys allows us to study the impact of increased chemical complexity and disorder when going from the binaries up to the quinaries. Note that the quaternary and quinary solid solutions have been confirmed experimentally as referenced in the beginning of the paragraph.

These equiatomic alloys were modeled using supercell models whose number of atoms is commensurate with the number of the elements of the alloys. Specifically, the binary and quaternary alloys were modeled using a 128-atom supercell ($4 \times 4 \times 4$ expansion of the two-atom conventional cell), the ternary alloys were modeled using 54-atom supercells ($3 \times 3 \times 3$ expansion of the two-atom conventional cell), and the quinary alloys were modeled using a 125-atom supercell ($5 \times 5 \times 5$ expansion of the one-atom primitive cell). Ideal chemical mixing of the elements was achieved utilizing the special quasirandom structure (SQS) approach [29]. Note that, although the supercell models for the ternary alloys have a smaller number of atoms, the employed SQSs well sample the local chemical environments around the atoms and hence provide good predictions of the atomic properties considered in this study (see Appendix C for details).

Atomic volumes, atomic charges, and atomic stresses were obtained based on the Bader charge analysis [24,25]. Bader regions are regions defined by boundaries for which the charge density gradient along the normal direction to the boundary surface is zero. Each Bader region is usually located at an atomic site. Occasionally, because of small fluctuations of the charge density, small Bader regions appear in interstitial regions. They are, however, almost negligible. The sum of local charges therein is at most 0.05% of the total charge. In practice, these small regions are assigned to an atom, to which the local charge maximum is the closest, to ensure that the sum of local values is equal to the corresponding quantity for the supercell. The Bader volume of each atom (V_{Bader}) is computed as the volume of the thus determined Bader region for the corresponding atom, and the Bader charge of each atom (ρ_{Bader}) is computed by integration of the charge density over V_{Bader}.

To compute atomic stresses we utilized the concept of stress densities. Electronic-structure-based stress densities have been widely used to analyze local properties, e.g., at grain boundaries [25,30–36], at surfaces [37–39], in superlattices [40], to analyze chemical bonding in molecules [41–43], in metal clusters [44–46], in metal complexes [47], in lithium-ionic conductors [48], and in Si-Fe [49], as well as to analyze electronic shell structures of atoms [50]. In the present study, the method by Filippetti and Fiorentini [51], later modified to fit the plane-wave basis projector augmented-wave (PAW) method [37], was employed to compute the stress density. The stress density $\sigma_{\alpha\beta}(\mathbf{r})$ satisfies

$$\sigma_{\alpha\beta} = \frac{1}{V}\int_V d\mathbf{r}\,\sigma_{\alpha\beta}(\mathbf{r}), \tag{1}$$

where α and β are indices for the Cartesian coordinates, $\sigma_{\alpha\beta}$ is the macroscopic stress tensor, and V denotes the simulation cell volume. Atomically resolved stress components were evaluated by integrating $\sigma_{\alpha\beta}$ within the Bader volumes of the corresponding atoms as

$$\sigma_{\mathrm{Bader},\alpha\beta} = \frac{1}{V_{\mathrm{Bader}}}\int_{V_{\mathrm{Bader}}} d\mathbf{r}\,\sigma_{\alpha\beta}(\mathbf{r}). \tag{2}$$

As discussed in Refs. [25,37], the gauge-dependent component can be eliminated by integrating $\sigma_{\alpha\beta}$ within the Bader volumes. For the sake of simplicity, in the present study, only the diagonal average of $\sigma_{\mathrm{Bader},\alpha\beta}$ was considered which we denote as σ_{Bader}. In the following, positive and negative values indicate compressive and tensile stresses, respectively.

For the integration over the Bader volumes required to obtain the Bader charge ρ_{Bader} and the average of the diagonal stress components σ_{Bader}, a weighted integration scheme [52] was applied to improve the convergence.

The QMAS code [40] was employed for electronic-structure calculations and for calculations of the Bader volumes, the Bader charges, and the Bader stresses. Electronic-structure calculations were conducted employing the PAW method [53] in the framework of density functional theory (DFT) within the generalized gradient approximation (GGA) of the Perdew-Burke-Ernzerhof (PBE) form [54]. The plane-wave cutoff energy was set to 20 Ha (544 eV). The Brillouin zones were sampled by Γ-centered $6 \times 6 \times 6$, $4 \times 4 \times 4$, $4 \times 4 \times 4$ k-point meshes for the 54-atom, 125-atom, 128-atom supercell models, and the Gaussian-smearing technique [55] was employed with the full width at half maximum (FWHM) smearing set to 25 meV. The calculations were performed at the DFT-determined equilibrium lattice constants (see Appendix A for details). The total energies were minimized until for each ionic step the charge differences became less than 10^{-8} per simulation cell, and internal atomic positions were relaxed until the residual forces became less than 5×10^{-5} Ha/bohr (2.5×10^{-3} eV/Å).

Valence-electron concentrations (VECs) of HEAs have been previously discussed in relation to phase stabilities [56–59]. In the present study, the VEC of each alloy was computed as the average of the VECs of the constituent elements weighted by their concentrations in atomic percent, where the VECs of the elements in groups 4, 5, and 6 were taken as 4, 5, and 6, respectively.

III. RESULTS AND DISCUSSION

A. Distributions of atomic volumes, charges, and stresses

Figure 1(a) shows the distributions of the atomic volumes V_{Bader} obtained from the Bader analysis for each element in the investigated equiatomic bcc alloys. For a given element (fixed column), the volume distributions and their averages depend on the considered alloy, with variations even up to 6.5 Å^3 in the averages. These variations are likely a consequence of the different equilibrium volumes of the alloys (solid gray lines), which are determined by the specific alloy composition. For a

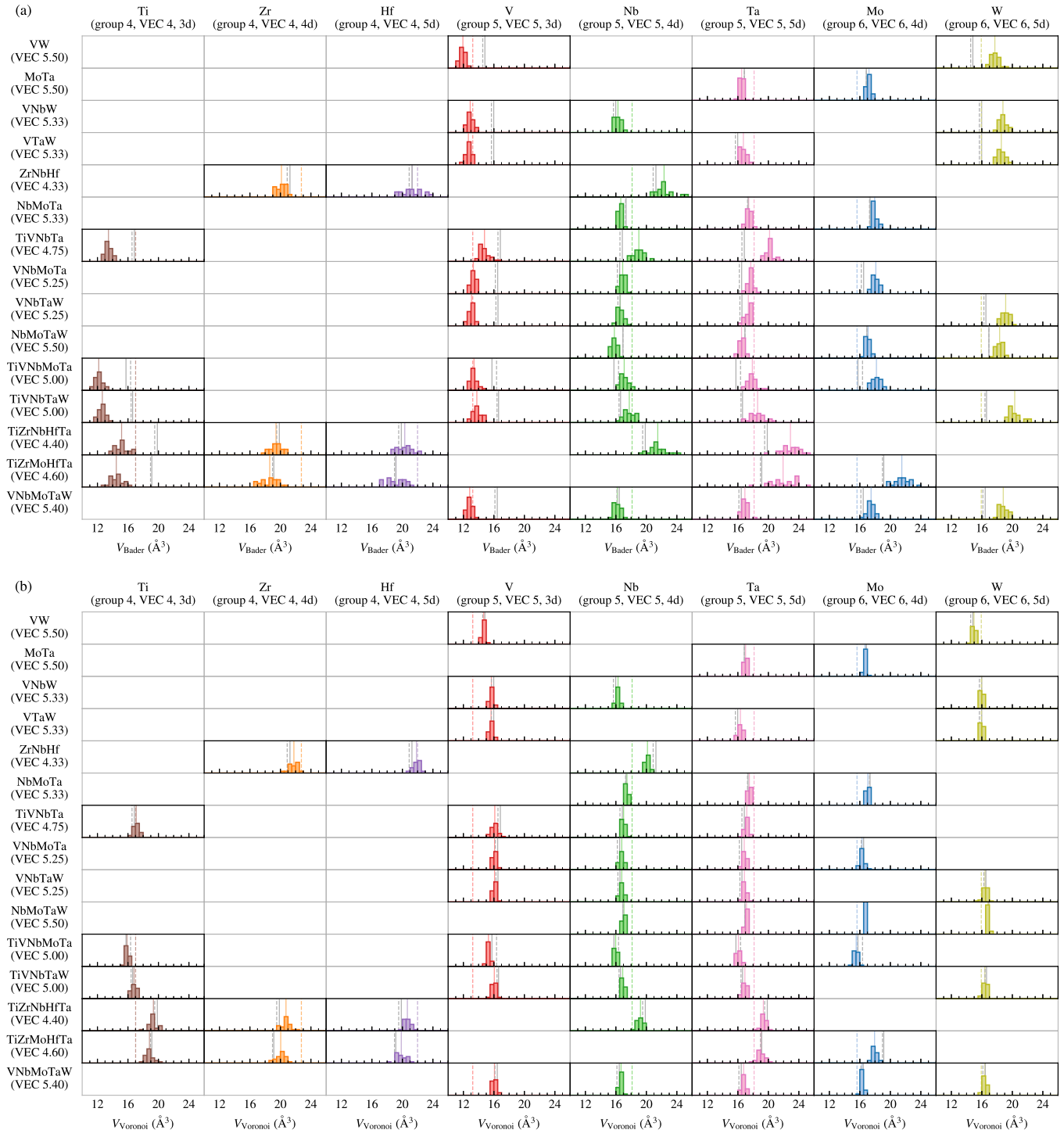

FIG. 1. Distributions of atomic volumes (a) V_{Bader} and (b) V_{Voronoi} (in Å^3) in the investigated equiatomic bcc alloys. The rows and the columns denote the alloys and the elements, respectively. The vertical solid gray lines show the equilibrium volume (per atom) of each alloy as obtained from the present DFT calculations. The vertical dashed gray lines indicate an approximate "equilibrium" volume (per atom) as obtained from Vegard's law, i.e., by the weighted average over the alloys' individual constitutive elements. Note that both gray lines, solid and dashed, mark exactly the same value in each row, i.e., alloy. The vertical dashed colored lines show the equilibrium volumes of the corresponding pure elements in the bcc phase, i.e., they mark the same value in each column. The vertical solid colored lines show the averaged atomic volumes as obtained here from the DFT calculated atomic volume distributions.

given alloy (fixed row), the average volumes of the different elements likewise show strong variations of up to 7.7 Å^3. This behavior indicates, as could be anticipated, that the individual atomic volumes depend on the type of the element. A much more revealing finding is that the atomic volumes of the *same* element in the *same* alloy show a large distribution (colored histogram bars) with standard deviations of up to 1.6 Å^3. This indicates clearly that the local atomic volumes depend not

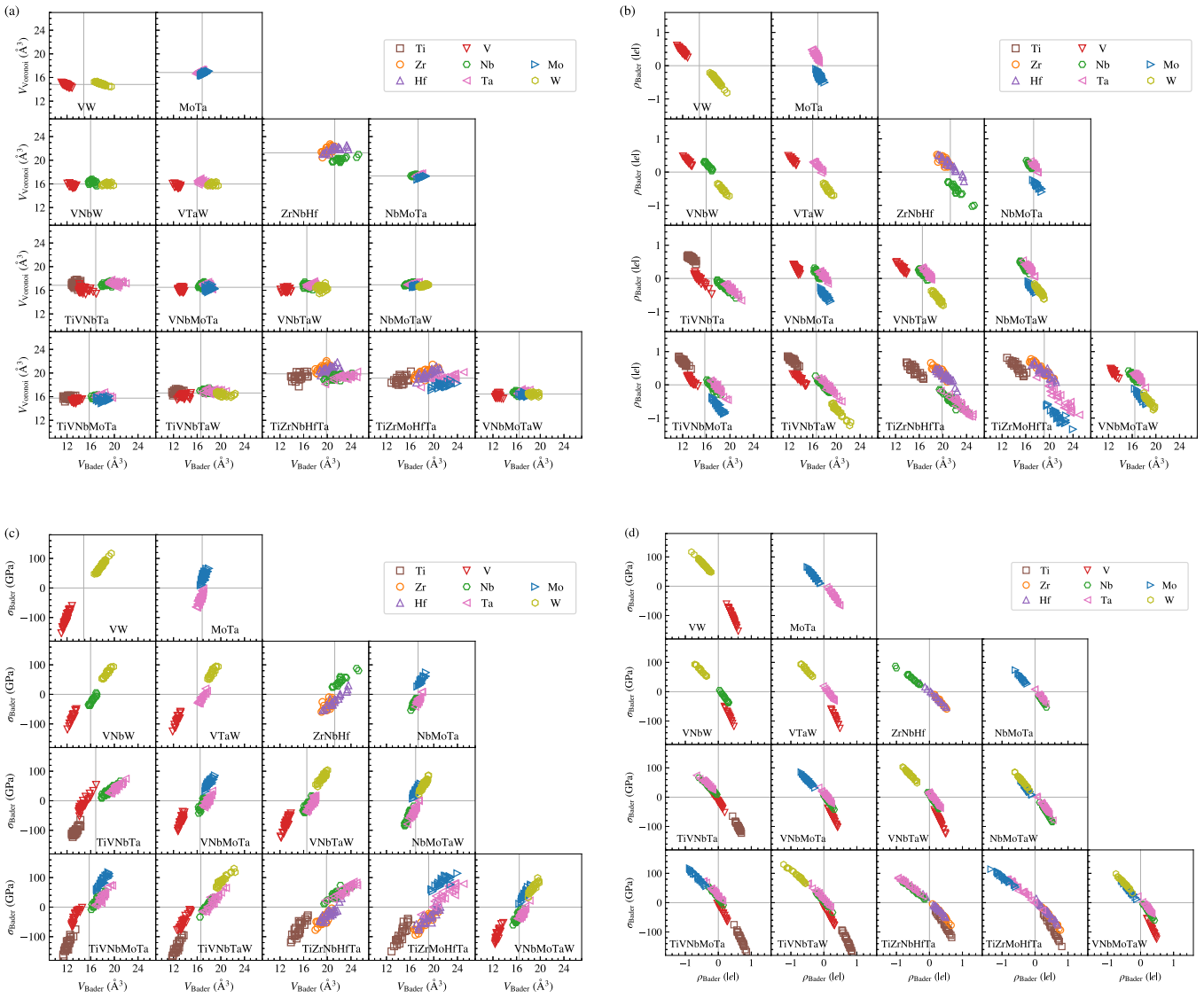

FIG. 2. Correlation plots for the various computed atomic properties, with binaries in the first, ternaries in the second, quaternaries in the third, and quinaries in the fourth row of each subfigure. (a) V_{Voronoi} vs V_{Bader}. The gray vertical and horizontal lines show the volumes of the alloys. No obvious correlation between the two types of atomic volume definition can be observed. (b) V_{Bader} vs ρ_{Bader}. The gray vertical lines show the volumes of the alloys. (c) V_{Bader} vs σ_{Bader}. (d) ρ_{Bader} and σ_{Bader}. In (b) through (d) clear linear correlations can be found.

only on the element and the overall alloy composition, but also very sensitively on the specific *local* chemical environment. A similar observation was made previously for atomic bond distances in fcc HEAs [18,21,60].

Furthermore, we can draw a relation between the average atomic Bader volumes and the corresponding atomic VECs. For a given alloy, the elements of the same period from the Periodic Table show decreasing average volumes with decreasing VEC (compare, e.g., Nb with Mo or Ta with W in the NbMoTaW HEA). It needs to be emphasized that this trend is opposite to the trend valid for the atomic volumes of pure metals. For the latter, it is known empirically (e.g., Slater [61] or Pauling [62]) and observed explicitly in our calculations (cf. dashed colored lines) that the atomic volumes increase with decreasing VEC. The discrepancy between the pure-metal atomic volumes and the Bader atomic volumes of the alloys is related to different local chemical environments in the solid solutions. Nonetheless, a rather simple Vegard's law (i.e., prediction of the alloy's volume by a linear mixing of the pure-metal atomic volumes) still works very well for all of the alloys. This indicates that there is a compensating effect among the constituent elements.

An apparently appealing alternative to a Bader volume analysis is based on atomic volumes obtained by a Voronoi tessellation which requires only structural input instead of electronic charge densities. Figure 1(b) shows the distribution of the Voronoi volumes (V_{Voronoi}) for the investigated alloys. Inspection of Fig. 1(b) in comparison to Fig. 1(a) reveals significant differences between the Bader and Voronoi volume distributions. A main difference which applies to all alloys and elements is that the Voronoi volumes show a much smaller standard deviation of the distributions (up to 0.6 Å^3). A more detailed comparison reveals further that the averages of the distributions strongly differ for many of the elements.

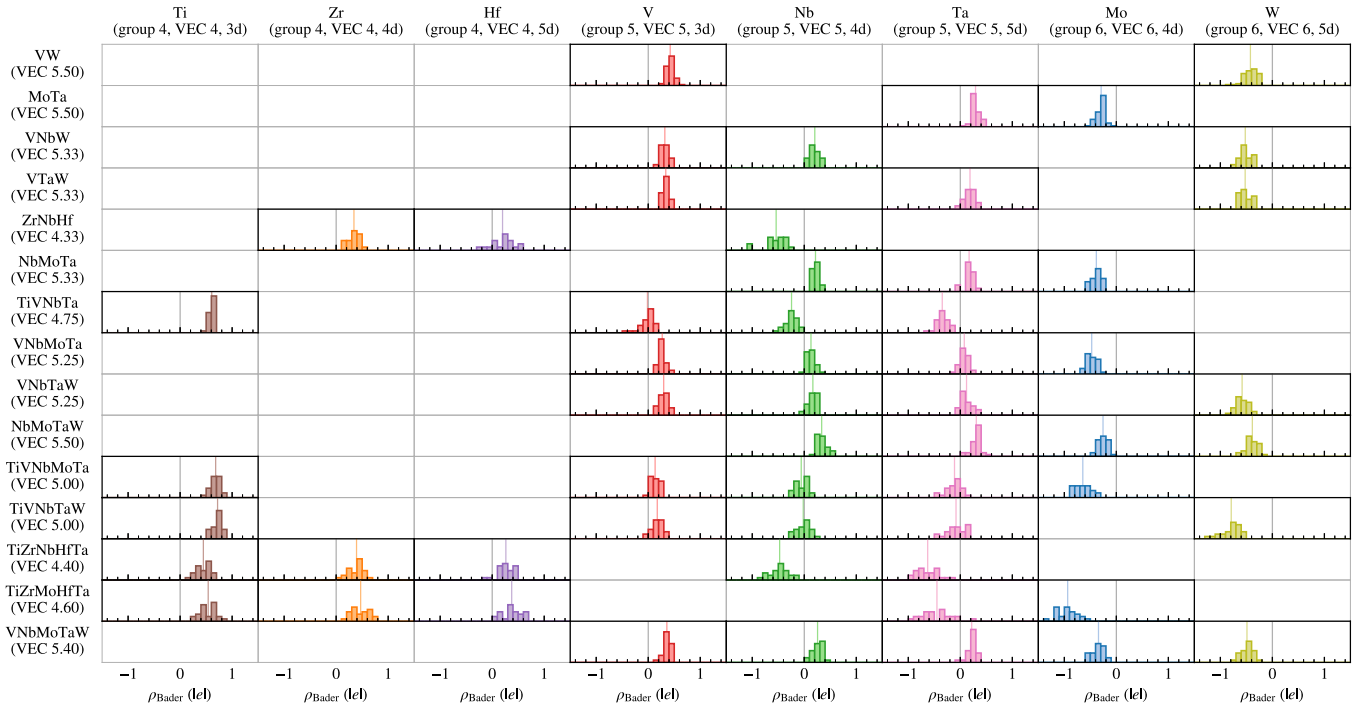

FIG. 3. Distributions of atomic charges ρ_{Bader} (in elementary charge units) in the investigated equiatomic bcc alloys. The rows and the columns denote the alloys and the elements inside, respectively. The vertical dashed gray lines indicate the neutral charge ($\rho_{\text{Bader}} = 0$). The vertical solid colored lines show the averaged atomic charges as obtained here from the DFT calculated atomic charge distributions.

Figure 2(a) highlights the differences between the Bader and Voronoi volumes explicitly by showing no obvious correlation between V_{Bader} and V_{Voronoi} for any of the elements in any of the alloys. These results clearly indicate that the two definitions of atomic volumes capture different characteristics of the atoms. This also implies that the Bader and the Voronoi volumes could be used as distinct descriptors for, e.g., modeling the solid-solution strengthening in HEAs.

Figure 3 shows the distributions of the atomic charges ρ_{Bader} obtained from the Bader analysis for each element in the investigated equiatomic bcc alloys. A wide spread of the distributions can be observed for each element in each of the alloys similarly as for the atomic Bader volumes shown in Fig. 1(a). In fact, there is a strong linear negative correlation between the Bader volumes and charges as clarified by Fig. 2(b). Specifically, a positive ρ_{Bader} indicates less electrons and results in a smaller V_{Bader}. For a given alloy, we observe that up to about one electron of charge can be transferred between the different elements. Further, for a given alloy, the elements with higher VEC tend to have negative charges, and also the elements in later periods in the Periodic Table tend to show more negative charges.

One may have expected that the charge transfer can be qualitatively predicted by electronegativities as defined, e.g., by Pauling [63] or by Allen [64–66], but the present results reveal a few exceptions. Taking the example of VW, Fig. 3 shows that V and W are charged positively and negatively, respectively, which is opposite to what is expected from Allen electronegativities of the two elements. In contrast, the correlation between the VEC and the Bader charge still holds in such alloys, indicating that the VEC is a good descriptor for the Bader charge (see Sec. III D for further analyses). Note that a similar correlation has been also found between local VEC and C solution energies in CrMnFeCoNi [67].

Figure 4 shows the distributions of the atomic stresses σ_{Bader} obtained from the Bader analysis for each element in the investigated equiatomic bcc alloys. A very similar picture arises as for the atomic volumes and atomic charges, in particular the atomic stresses are substantially distributed for each element in each alloy. Noteworthy, the local stresses experienced by the atoms are remarkably high—100 GPa and above. These values are even higher than those reported previously for fcc FeCoNi and CrFeCoNi [22], indicating larger local stresses in refractory bcc HEAs than in $3d$-transition-element fcc HEAs. The computed atomic stresses are also substantially higher than those at dislocation cores in bcc Fe [68,69], fcc Al [70], and B2 TiNi [71] as well as higher than the atomic stresses at grain boundaries of bcc Fe [30–32] and fcc Al and Cu [25,33–35].

Further, we find strong correlations between the Bader volumes and stresses [Fig. 2(c)] as well as between the Bader charges and stresses [Fig. 2(d)]. We can again draw a relation to the VECs. For a given alloy, the elements with lower VEC tend to show negative (tensile) stresses, and the elements with higher VEC tend to show positive (compressive) stresses. This trend is consistent with what is expected from V_{Bader}; for a given alloy, the elements with larger V_{Bader} tend to show more positive (compressive) stresses, and vice versa. The observed results for the atomic stresses are consistent with previous works for fcc alloys. Strong distributions of atomic pressures were also found for fcc FeCoNi and CrFeCoNi [22]. Strong correlations between atomic charges and atomic pressures were found for CrMnFeCoNi-based fcc equiatomic alloys [23].

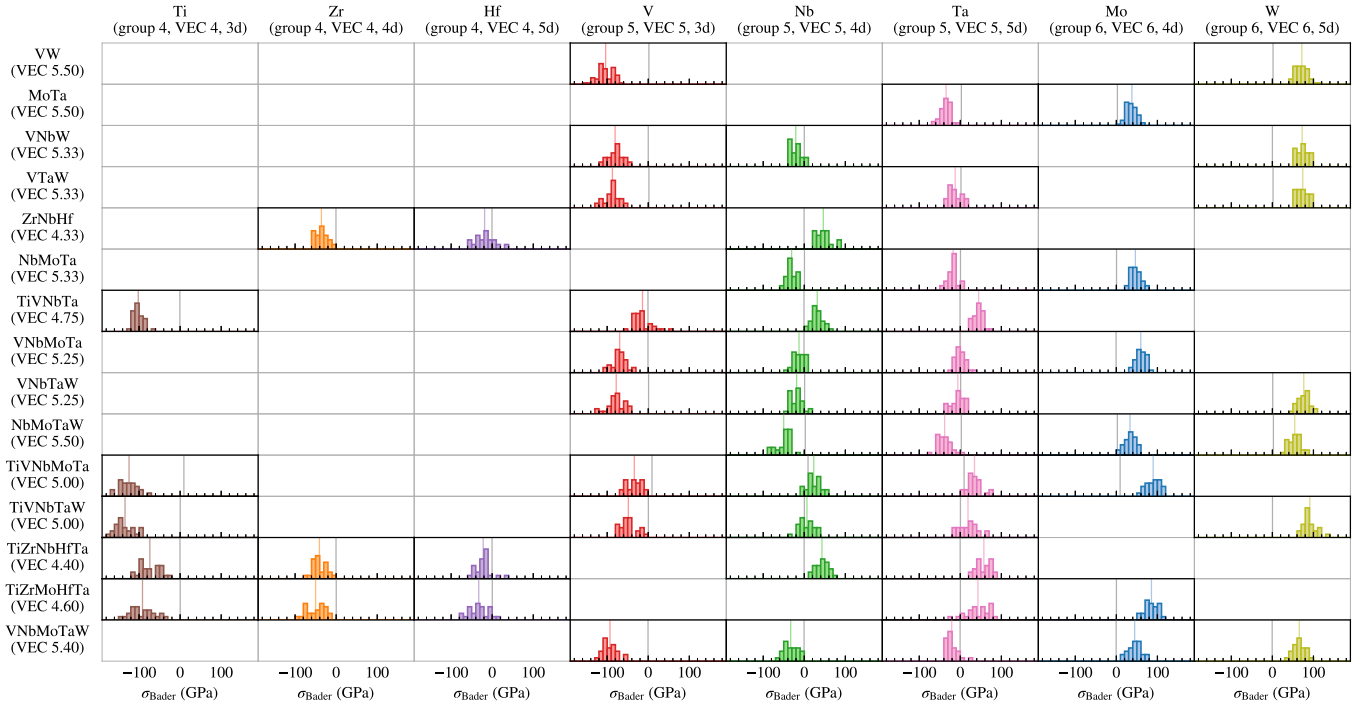

FIG. 4. Distributions of atomic stresses σ_{Bader} (in GPa) in the investigated equiatomic bcc alloys. The rows and the columns denote the alloys and the elements inside, respectively. The vertical dashed gray lines indicate the residual stresses of the alloys, which are close to zero. The vertical solid colored lines show the averaged atomic stresses as obtained here from the DFT calculated atomic stress distributions.

A previous work [17] reported that the RMS of the atomic displacements from the ideal lattice sites correlates with the yield strength normalized by the shear modulus for fcc CrMnFeCoNi-based HEAs. We therefore analyze the distributions of atomic displacements from the ideal lattice sites for each element in the investigated equiatomic bcc alloys. The

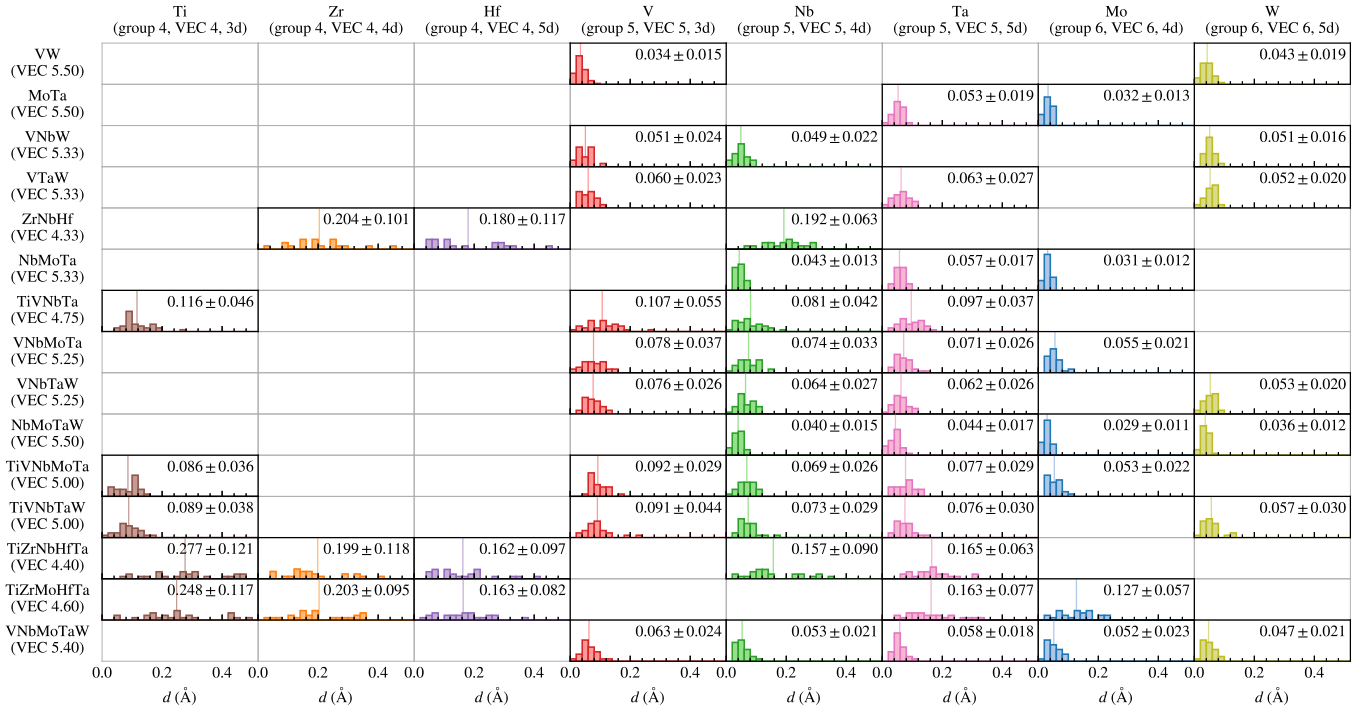

FIG. 5. Distributions of atomic displacements d (in Å) in the investigated equiatomic bcc alloys. The rows and the columns denote the alloys and the elements inside, respectively. The average and the standard deviation are also shown in each panel. The vertical solid colored lines show the averaged atomic displacements as obtained here from the DFT calculated atomic displacement distributions.

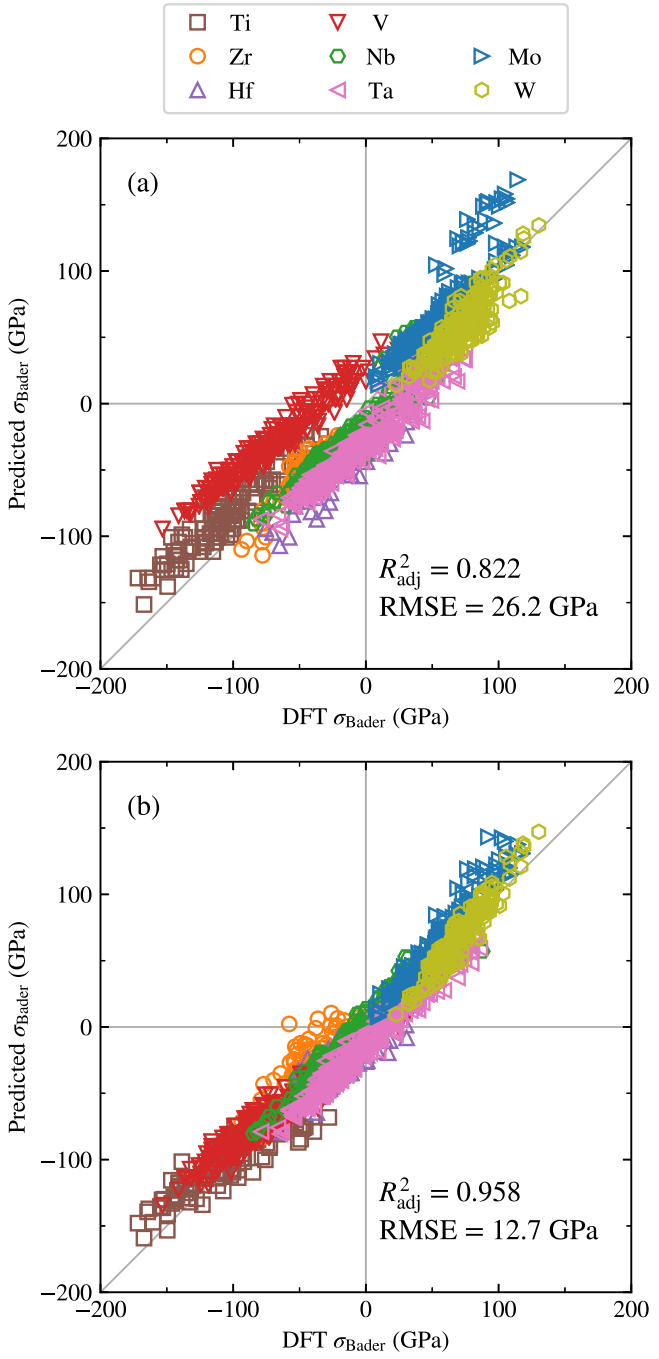

FIG. 6. Comparison between the DFT-computed Bader atomic stresses σ_{Bader} and those predicted from the linear-regression models for all the atoms in all the investigated alloy models. Panels (a) and (b) are based on Eqs. (7) and (8), respectively. The obtained R^2_{adj} and the root-mean-squared errors (RMSEs) are also shown in the panels.

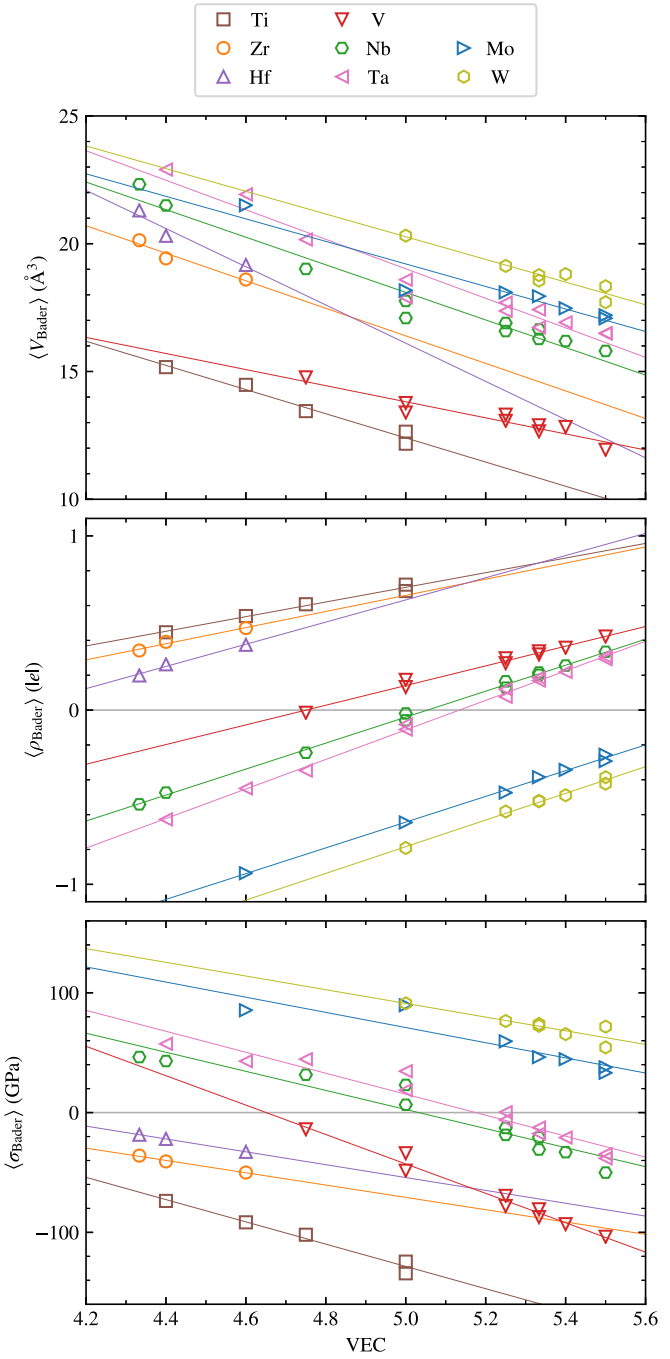

FIG. 7. Average atomic volume $\langle V_{\mathrm{Bader}} \rangle$ (top), average atomic charge $\langle \rho_{\mathrm{Bader}} \rangle$ (middle), and average atomic stress $\langle \sigma_{\mathrm{Bader}} \rangle$ (bottom) over individual elements as a function of the VEC of the alloys. The colored lines show the linear regression results for each element, whose coefficients are summarized in Table I.

atomic displacement of the ith atom d_i is computed as

$$d_i = \left| \mathbf{r}_i - \mathbf{r}_i^{\mathrm{ideal}} \right|, \tag{3}$$

where $\mathbf{r}_i^{\mathrm{ideal}}$ and $\mathbf{r}_i$ denote the internal atomic position of the ith atom at the ideal lattice sites and after the relaxation, respectively. Note that the reference ideal lattice is set to satisfy $\sum_i (\mathbf{r}_i - \mathbf{r}_i^{\mathrm{ideal}}) = 0$. Figure 5 shows the results. Particularly large displacements are found in ZrNbHf, TiZrNbHfTa, and TiZrMoHfTa, which include 60% or more of group-4 elements (Ti, Zr, Hf). This is probably because the bcc phase of the group-4 elements is known to be dynamically unstable at low temperatures [72–75], and hence the group-4 elements do not prefer to be located at the ideal bcc lattice sites at 0 K in DFT simulations. ZrNbHf and TiZrMoHfTa show in fact relatively low phonon frequencies compared with other refractory-element based alloys [76,77], indicating again less dynamical stability of these alloys in the bcc phase. The

dynamically unstable group-4 elements cause large displacements, i.e., large local lattice distortions. Consequently, not only the group-4 elements but also Nb and Ta show large displacements due to the large local lattice distortions around the atoms, even though Nb and Ta themselves favor ideal bcc lattice sites in their elemental states. The relatively large lattice distortions in ZrNbHf, TiZrNbHfTa, and TiZrMoHfTa may also affect V_{Bader}, ρ_{Bader}, and σ_{Bader}; in these alloys, relatively large distributions are found for the atomic properties (Figs. 1, 3, and 4).

B. Dependence of the distributions on the local environment

A main outcome of the analysis performed in Sec. III A is the widespread distribution of all investigated atomic properties V_{Bader}, ρ_{Bader}, and σ_{Bader}—even when considering the same element in any of the alloys. In order to shed light on the origin of these distributions, we now analyze their relation to the local chemical environments which are known to affect various properties of HEAs such as, e.g., stacking-fault energies (SFEs) or chemical short and long-range order [12,78–93].

To this end we perform a linear regression of the atomic properties as a function of the local composition around each atom. Since the atomic stresses are most relevant for mechanical properties [23] we focus here on σ_{Bader}. We have verified that similar results hold for V_{Bader} and ρ_{Bader}. The first, second, and third nearest-neighbor (NN) shells of the atoms, which include 8, 6, and 12 atoms, respectively, are considered. The compositional dependence of σ_{Bader} is fitted to the following linear equation:

$$\sigma_{\mathrm{Bader}} = a_0 + \sum_{i=1}^{N-1} \sum_{j} a_{i,j} x_{i,j}, \tag{4}$$

where $x_{i,j}$ denotes the concentration of the ith element in the jth nearest neighbor shell, N the number of elements in the alloy, and a_0 and $a_{i,j}$ linear regression coefficients. Note that, for an N-component alloy, the concentrations of only $N-1$ elements are independent for each shell, and therefore the summation over the elements in Eq. (4) runs only up to $N-1$. To evaluate the regression quality, the following adjusted coefficients of determination R^2_{adj} are employed:

$$R^2_{\mathrm{adj}} = 1 - (1 - R^2)\frac{n-1}{n-p-1}, \tag{5}$$

where p is the total number of explanatory variables and n is the sample size. The coefficient of determination R^2 is computed as

$$R^2 = 1 - \frac{\sum_{i=1}^{n}(y_i - f_i)^2}{\sum_{i=1}^{n}(y_i - \bar{y})^2}, \tag{6}$$

where y_i and f_i are the raw and the predicted values of the i th data point, respectively, and $\bar{y}$ is the mean value of $\{y_i\}$. R^2 is equal to 1 when the model is perfect and decreases when the regression becomes worse. Unlike R^2, it is possible that R^2_{adj} decreases when increasing the number of explanatory variables, indicating overfitting.

The resultant R^2_{adj} values from the linear regressions with Eq. (4) are shown in Table III (Appendix B). For a few alloys (MoTa, NbMoTa, NbMoTaW), already the first shell (1NN rows) provides an excellent description of the local chemical environment. Inclusion of the second shell into the regression (1 + 2NN rows) provides a very good description of the local environment for most of the alloys. A clear exception is ZrNbHf for which R^2_{adj} is only 0.370 and 0.729 for Zr and Hf, respectively. This may be attributed to the large structural distortions in this alloy, as demonstrated by the local atomic displacements in Fig. 5. When considering up to the 3NN shell, R^2_{adj} does not increase significantly; for some cases, it becomes even smaller indicating overfitting. We can conclude that σ_{Bader} can be well described and predicted based on the local compositions up to the 2NN shell.

In Sec. III A, we have indicated the correlation of the DFT computed atomic properties with the VEC at several places. It seems natural to ask whether these correlations can be quantified further. We thus investigate the following linear-regression model with the VEC as the variables:

$$\sigma_{\mathrm{Bader}} = a'_0 + a'_{1\mathrm{NN}}\,\Delta\mathrm{VEC}_{1\mathrm{NN}} + a'_{2\mathrm{NN}}\,\Delta\mathrm{VEC}_{2\mathrm{NN}}, \tag{7}$$

where $\Delta\mathrm{VEC}_{1\mathrm{NN}}$ and $\Delta\mathrm{VEC}_{2\mathrm{NN}}$ are the differences of the local VEC in the 1NN and the 2NN shells from the VEC

TABLE I. Linear regression results of the elementwise-averaged atomic properties $\langle V_{\mathrm{Bader}}\rangle$, $\langle \rho_{\mathrm{Bader}}\rangle$, and $\langle \sigma_{\mathrm{Bader}}\rangle$ as a linear function of the VEC of the alloys [Eq. (9)]. The column VEC_M shows the VEC for the elements. The columns y_M show the predicted values when VEC of the elements are given in Eq. (9). The columns R^2 show the coefficients of determination. Note that the results for Zr and Hf are obtained only from three alloys with low VECs, and the corresponding fits might hence be less predictable for high VECs than the results for the other elements.

		$y = \langle V_{\mathrm{Bader}}\rangle$ (Å^3)				$y = \langle \rho_{\mathrm{Bader}}\rangle$ ($\lvert e\rvert$)				$y = \langle \sigma_{\mathrm{Bader}}\rangle$ (GPa)			
M	VEC_M	a	b	y_M	R^2	a	b	y_M	R^2	a	b	y_M	R^2
Ti	4	−4.73	36.05	17.13	0.973	0.420	−1.398	0.284	0.983	−93.0	336.3	−35.5	0.975
Zr	4	−5.39	43.33	21.78	0.945	0.463	−1.656	0.196	0.978	−51.4	186.2	−19.4	0.990
Hf	4	−7.48	53.49	23.58	0.943	0.637	−2.550	−0.004	0.985	−53.7	214.1	−0.6	1.000
V	5	−3.15	29.55	13.82	0.902	0.564	−2.681	0.141	0.986	−122.7	570.8	−42.9	0.975
Nb	5	−5.40	45.08	18.10	0.956	0.745	−3.767	−0.040	0.998	−79.6	400.7	2.6	0.917
Ta	5	−5.77	47.89	19.02	0.948	0.848	−4.352	−0.114	0.997	−87.5	453.0	15.3	0.933
Mo	6	−4.41	41.25	14.80	0.896	0.739	−4.337	0.096	0.997	−63.3	387.4	7.7	0.825
W	6	−4.44	42.47	15.83	0.908	0.766	−4.612	−0.019	0.990	−57.1	376.7	34.0	0.781

of the center atom, respectively. In writing Eq. (7) we have used the recognition of the above regression results to restrict the parameters up to the second shell. Note, however, that the regression model of Eq. (7) is simpler than the one of Eq. (4) in that it contains only two linear-regression parameters. The model accuracy is tested by cross-validation (see Appendix C for details).

The results of the linear regressions with Eq. (7) are summarized in Table IV (Appendix B). In most cases, R^2_{adj} is over 0.8, indicating good predictive capability using just the two parameters, $\Delta\text{VEC}_{1\text{NN}}$ and $\Delta\text{VEC}_{2\text{NN}}$. Exceptions are found for group-4 elements in ZrNbHf, TiVNbTa, and TiZrMoHfTa; R^2_{adj} is at most about 0.75. The less accurate fits may be caused, as already discussed above, by the larger local lattice distortions for these alloys (Fig. 5). The slightly reduced R^2_{adj} compared with the regression model based on the local compositions, i.e., Eq. (4), should be attributed to the residual chemical differences among the chemical elements in the same group, which cannot be captured by the VEC alone. Comparing $a'_{1\text{NN}}$ and $a'_{2\text{NN}}$, the former is substantially larger than the latter, indicating that the 1NN shell has a stronger impact on σ_{Bader} than the 2NN shell, as intuitively expected. The main conclusion based on this analysis is that, given that local lattice distortions are not too strong, the local atomic properties can be well parametrized by local model Hamiltonians including the first two shells.

C. Universal models for a prediction of σ_{Bader}

In Sec. III B, we have expounded the good performance of $\Delta\text{VEC}_{1\text{NN}}$ and $\Delta\text{VEC}_{2\text{NN}}$ in predicting σ_{Bader} for the different alloys and elements separately. Here we would like to generalize the linear-regression model in order to make it applicable not only for a specific alloy composition, but rather universally to the class of bcc refractory alloys.

For that purpose we again apply Eq. (7); however, now not for the individual alloys and elements, but instead taking the data of all the 1609 atoms in all the investigated alloys as input to a single fit. The model accuracy is tested by cross-validation (Appendix C). For σ_{Bader}, the such obtained linear-regression coefficients are

$$\begin{aligned} a'_0 &= -6.7\ \text{GPa}, \\ a'_{1\text{NN}} &= -79.7\ \text{GPa}, \\ a'_{2\text{NN}} &= -21.6\ \text{GPa}. \end{aligned}$$

The R^2_{adj} value is 0.822, indicating a rather good predictive capability of the fit even when using only the two descriptors $\Delta\text{VEC}_{1\text{NN}}$ and $\Delta\text{VEC}_{2\text{NN}}$. Figure 6(a) compares the thus predicted σ_{Bader} values with the original DFT values. The data points are found to be divided into several subgroups, which can be assigned to the different element types.

Based on this result, we anticipate that the predictive power of the model can be improved upon inclusion of element-specific information. Thus we next introduce the DFT-computed pure-metal atomic volumes $\tilde{V}$ listed in Table II (Appendix A) into the fitting procedure. Specifically, we compute the averages of $\tilde{V}$ over the 1NN and 2NN shells of each atom and then subtract $\tilde{V}$ of the respective center atom ($\Delta\tilde{V}_{1\text{NN}}$ and $\Delta\tilde{V}_{2\text{NN}}$, respectively). The corresponding

TABLE II. Optimized lattice constants in the bcc phase (a_{bcc}) and corresponding atomic volumes (V). Available experimental and first-principles values obtained using the PBE functional are also shown.

	a_{bcc} (Å)	V (Å^3)	Method	Ref.
Ti	3.24	17.01	PBE	This study
V	2.98	13.23	PBE	This study
	2.763	10.54	Expt.	[95]
Zr	3.57	22.75	PBE	This study
Nb	3.31	18.13	PBE	This study
	3.303	18.02	Expt.	[95]
Mo	3.15	15.63	PBE	This study
	3.1460	15.57	Expt.	[26]
	3.146	15.58	Expt.	[95]
Hf	3.53	21.99	PBE	This study
Ta	3.31	18.13	PBE	This study
	3.3025	18.01	Expt.	[26]
	3.308	18.10	Expt.	[95]
W	3.17	15.93	PBE	This study
	3.165	15.86	Expt.	[95]
VW	3.095	14.82	PBE	This study
MoTa	3.23	16.85	PBE	This study
	3.2345	16.92	Expt.	[26]
VNbW	3.1735	15.98	PBE	This study
VTaW	3.1735	15.98	PBE	This study
ZrNbHf	3.490	21.25	PBE	This study
	3.467	20.83	PBE	[18]
	3.4884	21.22	Expt.	[27]
NbMoTa	3.261	17.34	PBE	This study
TiVNbTa	3.23	16.85	PBE	This study
	3.2193	16.68	Expt.	[6]
VNbMoTa	3.2075	16.50	PBE	This study
	3.208	16.51	Expt.	[5]
VNbTaW	3.21	16.54	PBE	This study
	3.2186	16.67	Expt.	[6]
NbMoTaW	3.235	16.93	PBE	This study
	3.2134(3)	16.59	Expt.	[2]
	3.22	16.69	Expt.	[3]
TiVNbMoTa	3.158	15.75	PBE	This study
	3.213	16.58	PBE	[7]
	3.224	16.76	Expt.	[7]
TiVNbTaW	3.215	16.62	PBE	This study
	3.2244	16.76	Expt.	[6]
TiZrNbHfTa	3.412	19.86	PBE	This study
	3.406	19.76	PBE	[18]
	3.404(1)	19.72	Expt.	[4]
TiZrMoHfTa	3.370	19.14	PBE	This study
	3.376	19.24	Expt.	[28]
VNbMoTaW	3.204	16.45	PBE	This study
	3.193	16.27	PBE	[18]
	3.1832(2)	16.13	Expt.	[2]
	3.185	16.15	Expt.	[3]
	3.187	16.19	Expt.	[3]

linear-regression model therefore reads as

$$\begin{aligned} \sigma_{\text{Bader}} = a''_0 + a''_{1\text{NN}}\Delta\text{VEC}_{1\text{NN}} + a''_{2\text{NN}}\Delta\text{VEC}_{2\text{NN}} \\ + v''_{1\text{NN}}\Delta\tilde{V}_{1\text{NN}} + v''_{2\text{NN}}\Delta\tilde{V}_{2\text{NN}}. \end{aligned} \quad (8)$$

The model accuracy is tested by cross-validation (Appendix C). The resultant linear-regression coefficients

TABLE III. Adjusted coefficients of determination, R^2_{adj}, for the linear regression models based on Eq. (4) with different numbers of atomic shells included. The column "shells" denotes the considered shells, where 1NN, 1+2NN, and 1+2+3NN mean that the local composition up to the 1NN, the 2NN, and the 3NN shell is included in the linear regression model, respectively.

	Shells	Ti	Zr	Hf	V	Nb	Ta	Mo	W
VW	1NN				0.700				0.597
	1+2NN				0.973				0.976
	1+2+3NN				0.972				0.976
MoTa	1NN						0.987	0.993	
	1+2NN						0.987	0.993	
	1+2+3NN						0.988	0.993	
VNbW	1NN				0.774	0.710			0.628
	1+2NN				0.956	0.977			0.980
	1+2+3NN				0.981	0.976			0.976
VTaW	1NN				0.769		0.669		0.621
	1+2NN				0.952		0.962		0.987
	1+2+3NN				0.975		0.961		0.986
ZrNbHf	1NN		0.365	0.761		0.866			
	1+2NN		0.369	0.729		0.928			
	1+2+3NN		0.635	0.731		0.922			
NbMoTa	1NN					0.951	0.910	0.955	
	1+2NN					0.988	0.996	0.994	
	1+2+3NN					0.994	0.997	0.998	
TiVNbTa	1NN	0.534			0.742	0.664	0.594		
	1+2NN	0.857			0.954	0.959	0.940		
	1+2+3NN	0.848			0.951	0.958	0.934		
VNbMoTa	1NN				0.854	0.818	0.849	0.832	
	1+2NN				0.991	0.980	0.979	0.980	
	1+2+3NN				0.993	0.978	0.979	0.978	
VNbTaW	1NN				0.871	0.601	0.790		0.736
	1+2NN				0.989	0.980	0.982		0.979
	1+2+3NN				0.991	0.978	0.981		0.979
NbMoTaW	1NN					0.947	0.948	0.904	0.922
	1+2NN					0.993	0.991	0.993	0.993
	1+2+3NN					0.994	0.993	0.995	0.993
TiVNbMoTa	1NN	0.806			0.822	0.600	0.676	0.804	
	1+2NN	0.960			0.959	0.961	0.967	0.974	
	1+2+3NN	0.973			0.959	0.962	0.969	0.972	
TiVNbTaW	1NN	0.668			0.685	0.660	0.620		0.805
	1+2NN	0.944			0.949	0.981	0.969		0.978
	1+2+3NN	0.947			0.936	0.981	0.960		0.986
TiZrNbHfTa	1NN	0.684	0.669	0.505		0.603	0.781		
	1+2NN	0.778	0.707	0.767		0.833	0.888		
	1+2+3NN	0.780	0.682	0.878		0.882	0.923		
TiZrMoHfTa	1NN	0.822	0.902	0.675			0.875	0.698	
	1+2NN	0.869	0.924	0.791			0.943	0.891	
	1+2+3NN	0.901	0.932	0.838			0.968	0.891	
VNbMoTaW	1NN				0.822	0.811	0.675	0.868	0.917
	1+2NN				0.956	0.984	0.973	0.994	0.987
	1+2+3NN				0.965	0.985	0.972	0.994	0.987

are

$$
\begin{aligned}
a''_0 &= -6.7\ \text{GPa},\\
a''_{1\text{NN}} &= -84.4\ \text{GPa},\\
a''_{2\text{NN}} &= -31.1\ \text{GPa},\\
v''_{1\text{NN}} &= -3.7\ \text{GPa/Å}^3,\\
v''_{2\text{NN}} &= -8.5\ \text{GPa/Å}^3.
\end{aligned}
$$

Figure 6(b) compares the such predicted σ_{Bader} values with the original DFT ones. The R^2_{adj} value is 0.958, indicating a substantial improvement of predictive power compared with the linear-regression model based on Eq. (7), and the data points from all the elements are almost on the same line.

It must be noted that, even though the two universal linear-regression models provide high R^2_{adj} values, it does not mean that these universal models have a predictive power as good as those obtained for the individual alloys and elements. The reason is that the less-predictable cases seen for

group-4 elements in element-and-alloywise models in Sec. III B and Table IV are smeared out in the universal models. The universal models should, nevertheless, be useful because they can be immediately applied to refractory alloys with, e.g., nonequiatomic compositions and/or chemical short-range order, without explicit DFT calculations, once their chemical configuration is given.

D. Relation to the averaged valence-electron concentration

The above analysis has shown a strong correlation between the computed atomic Bader properties and the VECs of the nearest neighbor shells. We show now that, by further data coarse graining, we are able to establish a simple linear relation between corresponding averaged properties.

Figure 7 shows the atomic properties averaged over the individual elements (denoted by angle brackets) as a function of the overall VEC of the considered alloys. For each element, the three investigated atomic quantities depend linearly on the alloys' VEC, almost independently of their actual chemical composition. The dependence of each atomic property on the VEC is qualitatively similar among the elements. Specifically, $\langle V_{\mathrm{Bader}}\rangle$ decreases, $\langle \rho_{\mathrm{Bader}}\rangle$ increases, and $\langle \sigma_{\mathrm{Bader}}\rangle$ decreases with increasing VEC. To quantify the dependence on the VEC, the results were fitted to a linear equation, i.e.,

$$y = a\mathrm{VEC} + b, \tag{9}$$

where y stands for the elementwise-averaged atomic property, i.e., $\langle V_{\mathrm{Bader}}\rangle$, $\langle \rho_{\mathrm{Bader}}\rangle$, and $\langle \sigma_{\mathrm{Bader}}\rangle$, and a and b are linear regression coefficients. Table I summarizes the obtained regression results. Among the three investigated quantities, $\langle \rho_{\mathrm{Bader}}\rangle$ shows particularly high coefficients of determination R^2 for all the elements, indicating a strong linear relation between ρ_{Bader} and the averaged VECs. It is also interesting that, when plugging the VECs of the constituent elements (VEC_M in Table I) into the linear regression model, the thus predicted values of $\langle V_{\mathrm{Bader}}\rangle$ approximately recover the equilibrium volumes of the pure metals (see Table II).

IV. CONCLUSIONS

We have analyzed atomic volumes, charges, and stresses in various equiatomic bcc refractory alloys ranging from binaries up to high-entropy alloys (HEAs) employing a Bader analysis. The atomic properties show unexpectedly large distributions even for the same element in the same alloy, indicating substantial impact from the local chemical environment. These atomic properties are also strongly linearly correlated with each other in each alloy and for each element, indicating the physical consistency among them as all are based on the same Bader analysis concept. The elementwise averages of the computed atomic properties are found to correlate well with the VEC of a given alloy. From coarse graining the atomistic data, the atomic stresses for each element are found to be well predicted by linear equations as functions of the local compositions or the VECs in the 1NN and 2NN shells. This quantitatively demonstrates that distributions of atomic stresses, as well as those of atomic volumes and atomic charges, originate from local chemical deviations from the equiatomic alloy composition. The findings clearly emphasize

TABLE IV. Linear regression coefficients a'_0, $a'_{1\mathrm{NN}}$, $a'_{2\mathrm{NN}}$ (in GPa), adjusted coefficients of determination R^2_{adj}, and root-mean-squared errors (RMSEs; in GPa) for the linear-regression model for σ_{Bader} in Eq. (7) for each element in each alloy.

	Alloy	a'_0	$a'_{1\mathrm{NN}}$	$a'_{2\mathrm{NN}}$	R^2_{adj}	RMSE
Ti	TiVNbTa	−24.8	−70.1	−32.8	0.649	6.9
	TiVNbMoTa	−9.9	−90.9	−22.8	0.888	6.9
	TiVNbTaW	−10.4	−93.9	−30.8	0.809	9.2
	TiZrNbHfTa	−15.9	−115.5	−27.7	0.721	12.7
	TiZrMoHfTa	−22.8	−96.2	−16.9	0.808	12.2
Zr	ZrNbHf	−0.1	−91.9	−15.8	0.420	10.5
	TiZrNbHfTa	−7.0	−76.4	−8.0	0.644	10.1
	TiZrMoHfTa	−5.0	−69.8	−5.3	0.894	7.3
Hf	ZrNbHf	17.6	−112.7	4.3	0.752	10.8
	TiZrNbHfTa	36.4	−99.9	−47.3	0.683	10.1
	TiZrMoHfTa	24.5	−77.9	−18.1	0.731	11.4
V	VW	−24.5	−104.3	−47.7	0.973	3.1
	VNbW	−28.6	−113.1	−43.2	0.937	4.2
	VTaW	−37.7	−111.9	−36.8	0.885	5.7
	TiVNbTa	−53.4	−101.9	−55.9	0.843	8.5
	VNbMoTa	−42.9	−88.7	−17.9	0.895	5.1
	VNbTaW	−41.0	−109.0	−39.2	0.944	4.6
	TiVNbMoTa	−34.8	−81.8	−25.8	0.902	5.5
	TiVNbTaW	−48.1	−91.2	−36.6	0.920	5.5
	VNbMoTaW	−46.1	−95.9	−20.6	0.866	6.1
Nb	VNbW	26.7	−89.1	−53.1	0.914	3.7
	ZrNbHf	−39.0	−99.4	−28.6	0.934	4.2
	NbMoTa	−3.5	−75.8	−6.2	0.954	2.2
	TiVNbTa	9.0	−61.7	−28.6	0.804	5.6
	VNbMoTa	10.4	−83.4	−9.6	0.841	5.2
	VNbTaW	14.8	−96.0	−37.7	0.811	6.1
	NbMoTaW	−3.0	−84.1	−10.0	0.964	3.1
	TiVNbMoTa	22.7	−73.0	−25.8	0.827	6.6
	TiVNbTaW	6.5	−83.6	−35.4	0.929	4.3
	TiZrNbHfTa	−30.0	−87.9	−33.1	0.822	6.5
	VNbMoTaW	6.8	−83.5	−16.0	0.806	6.5
Ta	MoTa	7.6	−83.9	1.3	0.987	1.5
	VTaW	39.1	−97.7	−56.9	0.844	5.6
	NbMoTa	11.5	−75.0	−12.4	0.959	2.4
	TiVNbTa	16.4	−79.9	−32.6	0.810	4.9
	VNbMoTa	29.0	−96.7	−17.8	0.842	4.8
	VNbTaW	28.2	−101.3	−35.8	0.908	4.7
	NbMoTaW	20.8	−101.2	−16.7	0.949	3.6
	TiVNbMoTa	34.2	−74.5	−25.4	0.834	7.2
	TiVNbTaW	19.2	−83.7	−42.1	0.884	7.6
	TiZrNbHfTa	−13.0	−89.7	−28.4	0.863	6.3
	TiZrMoHfTa	3.3	−83.1	−16.0	0.897	8.5
	VNbMoTaW	19.2	−73.4	−27.6	0.825	5.5
Mo	MoTa	−1.0	−75.1	−0.7	0.993	1.0
	NbMoTa	−8.4	−70.0	−12.1	0.974	1.9
	VNbMoTa	−0.8	−63.4	−17.0	0.877	4.2
	NbMoTaW	−13.6	−77.8	−15.8	0.950	2.8
	TiVNbMoTa	−4.0	−67.1	−27.3	0.921	4.6
	TiZrMoHfTa	−30.6	−64.7	−18.0	0.879	5.3
	VNbMoTaW	−23.9	−84.9	−29.9	0.938	3.9
W	VW	4.3	−80.5	−48.5	0.976	2.3
	VNbW	−0.2	−69.3	−39.6	0.934	3.1
	VTaW	−1.3	−74.6	−38.4	0.842	5.2
	VNbTaW	−3.4	−76.4	−30.1	0.887	4.4
	NbMoTaW	6.1	−81.1	−15.5	0.959	3.0
	TiVNbTaW	−15.3	−76.0	−30.5	0.940	4.0
	VNbMoTaW	7.7	−77.6	−18.0	0.897	4.7

TABLE V. Root-mean-squared errors (RMSEs; in GPa) of σ_{Bader} evaluated for the test sets using repeated k-fold cross validation for the linear regression model in Eq. (7) based on the local VEC. $k = 3$ for ternary and quinary alloys, while $k = 4$ for binary and quaternary alloys. The repeat count equals 10. In parentheses, the RMSEs for the whole sets, corresponding to Table IV, are shown.

	Ti	Zr	Hf	V	Nb	Ta	Mo	W
VW				3.2 (3.1)				2.4 (2.3)
MoTa						1.5 (1.5)	1.1 (1.0)	
VNbW				5.2 (4.2)	4.3 (3.7)			3.5 (3.1)
VTaW				6.8 (5.7)		6.8 (5.6)		6.0 (5.2)
ZrNbHf		12.0 (10.5)	12.9 (10.8)		5.2 (4.2)			
NbMoTa					2.6 (2.2)	2.8 (2.4)	2.2 (1.9)	
TiVNbTa	7.5 (6.9)			9.3 (8.5)	6.0 (5.6)	5.1 (4.9)		
VNbMoTa				5.5 (5.1)	5.8 (5.2)	5.3 (4.8)	4.5 (4.2)	
VNbTaW				4.9 (4.6)	6.8 (6.1)	5.1 (4.7)		4.9 (4.4)
NbMoTaW					3.3 (3.1)	3.9 (3.6)	3.1 (2.8)	3.1 (3.0)
TiVNbMoTa	7.7 (6.9)			6.2 (5.5)	7.3 (6.6)	8.1 (7.2)	5.4 (4.6)	
TiVNbTaW	10.8 (9.2)			6.1 (5.5)	4.9 (4.3)	8.5 (7.6)		4.7 (4.0)
TiZrNbHfTa	15.2 (12.7)	10.9 (10.1)	11.8 (10.1)		7.5 (6.5)	7.1 (6.3)		
TiZrMoHfTa	14.5 (12.2)	8.3 (7.3)	13.3 (11.4)			9.2 (8.5)	6.0 (5.3)	
VNbMoTaW				7.0 (6.1)	7.1 (6.5)	6.3 (5.5)	4.4 (3.9)	5.5 (4.7)

the importance of taking local chemical environments into account to analyze properties of disordered alloys.

The variation of the local atomic properties between the different elements in the same alloy can be very significant. The computed atomic Bader volumes can vary by several Å^3. From the Bader charges we could observe that up to about one electron of charge can be transferred between the different element types. The resulting Bader stresses showed a very remarkable local variation of the stresses acting on the atoms, in the range of 100 GPa. These local stress levels are significantly higher than those in fcc alloys and also higher than those in the vicinity of dislocation cores or at grain boundaries. The observed gigantic local stresses due to chemical disorder are therefore likely to impact the interaction among these atomic structural defects in chemically disordered alloys.

Atomic properties such as local atomic volumes have been successfully used as an input, e.g., for modeling solid-solution strengthening in HEAs. The physically consistent Bader-analysis-based atomic properties are found to be almost uncorrelated with Voronoi volumes. This indicates that the Bader and the Voronoi volumes capture different characteristics of the atoms and hence could be used as distinct descriptors when modeling the solid-solution strengthening in HEAs. Since the Bader-analysis-based atomic properties are also found to be well predicted based on local chemical compositions, it becomes possible to screen wide compositions to find, e.g., compositions with high strength without employing explicit and thus computationally expensive supercell calculations. The present insights into the correlation between the key descriptors can also be used to design coarse-grained descriptions of the electronic structure (e.g., tight binding or bond order potentials [94]) for such chemically complex alloy systems.

ACKNOWLEDGMENTS

We thank Andrei V. Ruban for sharing his code to generate the SQSs. This work was supported by "Materials research by Information Integration" Initiative (MI^{2}I) project of the Support Program for Starting Up Innovation Hub from JST, by MEXT as a social and scientific priority issue (creation of new functional devices and high-performance materials to support next-generation industries; CDMSI) to be tackled by using post-K computer, by the German Research Foundation (DFG) under the priority programme "Compositionally Complex Alloys - High Entropy Alloys (CCA - HEA)" (SPP 2006), by Netherlands Organization for Scientific Research (NWO) under VIDI Grant No. 15707, and by the European Union's Horizon 2020 research and innovation programme (Grant Agreement No. 639211).

APPENDIX A: OPTIMIZATION OF LATTICE CONSTANTS

Before performing the analysis of the local atomic properties discussed in the main text, we first determined the lattice constants of the investigated refractory alloys employing the VASP code [96–98]. The plane-wave basis PAW method [53] was employed with the GGA of the PBE form [54]. The plain-wave energy cutoff was set to 400 eV. The Brillouin zones were sampled by Γ-centered $6 \times 6 \times 6$, $4 \times 4 \times 4$, $4 \times 4 \times 4$ k-point meshes for the 54-atom, 125-atom, 128-atom supercell models, and the Methfessel-Paxton scheme [99] was employed with a smearing width of 0.1 eV. The total energies were minimized until the energy differences became less than 10^{-3} eV per simulation cell for each ionic step, and internal atomic positions were relaxed until the residual forces became less than 5×10^{-2} eV/Å. Several volumes were first computed with relaxing the internal atomic positions from the ideal lattice sites. The equilibrium lattice constants were then obtained by fitting the energy–volume relations to the Vinet equation of state [100]. Table II shows the obtained lattice constants.

APPENDIX B: RESULTS OF LINEAR REGRESSION

Adjusted coefficients of determination, R^2_{adj}, for the linear regression model corresponding to Eq. (4) are listed in Table III. The linear regression coefficients, a'_0, $a'_{1\text{NN}}$, $a'_{2\text{NN}}$,

TABLE VI. Root-mean-squared errors (RMSEs; in GPa) of σ_{Bader} for the linear regression model in Eq. (7) based on the local VEC applied to the permuted chemical configurations for the ternary alloys. The first configuration *ABC* is used for constructing the linear regression model (hence these values correspond to the respective ones in Table IV), while the other five configurations are *not* used for the training of the regression model.

	ABC			*BCA*			*CAB*			*ACB*			*CBA*			*BAC*		
ABC	*A*	*B*	*C*	*A*	*B*	*C*	*A*	*B*	*C*	*A*	*B*	*C*	*A*	*B*	*C*	*A*	*B*	*C*
VNbW	4.2	3.7	3.1	4.9	4.5	2.3	2.8	4.4	3.3	3.8	5.0	3.5	4.4	4.7	3.8	4.0	3.9	3.8
VTaW	5.7	5.6	5.2	7.5	6.6	3.5	4.1	6.5	3.9	5.7	8.1	4.3	6.4	6.9	4.5	6.1	5.6	6.0
ZrNbHf	10.5	4.2	10.8	11.7	5.7	10.5	14.8	6.2	12.8	12.7	7.4	9.6	12.2	6.5	12.0	11.0	6.2	12.1
NbMoTa	2.2	1.9	2.4	2.5	1.6	1.7	2.7	2.3	2.2	2.0	2.5	2.6	3.1	2.2	2.6	1.9	2.0	2.8

adjusted coefficients of determination, R^2_{adj}, and root-mean-squared errors (RMSEs) for the linear regression model corresponding to Eq. (7) are listed in Table IV.

APPENDIX C: QUALITY OF THE LINEAR REGRESSION MODELS

In order to examine the quality of the linear regression model in Eq. (7) for the individual alloys and elements based on the local valence electron concentration (VEC), we performed a repeated k-fold cross-validation analysis. The k value was set to 3 for ternary and quinary alloys, and to 4 for binary and quaternary alloys. The repeat count was 10. The resultant RMSEs of σ_{Bader} for the test sets are listed in Table V. There is no significant degradation compared with the RMSEs for the whole data sets (given in parentheses and corresponding to Table IV) demonstrating no overfitting and hence a good predictive power of the linear regression models. This also indicates that the present supercells well sample different local chemical environments, i.e., they are converged with respect to the supercell size.

To further test the transferability of the linear regression model in Eq. (7), we applied the obtained fits to chemical configurations *not* used for the training. The new configurations were constructed by permuting the chemical elements in the SQS models. For ZrNbHf, for example, a new distinct chemical configuration "NbHfZr" can be obtained by replacing Zr with Nb, Nb with Hf, and Hf with Zr. The internal atomic positions of the such obtained new chemical configurations were relaxed and then σ_{Bader} was computed. Table VI shows the RMSEs of σ_{Bader} for the supercell models with the permuted chemical configurations for the ternary alloys. No significant degradation is found for the RMSEs compared with the original configurations (*ABC*). This, again, indicates a good transferability of the linear regression model in Eq. (7).

We also performed a 10-times repeated eightfold cross-validation analysis for the universal models corresponding to Eqs. (7) and (8) in Sec. III C. The resultant RMSEs are 26.2 GPa and 12.8 GPa, respectively. These values are basically the same as the RMSEs obtained for the whole data sets (i.e., 26.2 GPa and 12.7 GPa as also given in Fig. 6), clearly indicating no overfitting.

[1] O. N. Senkov, D. B. Miracle, K. J. Chaput, and J.-P. Couzinie, J. Mater. Res. **33**, 3092 (2018).
[2] O. Senkov, G. Wilks, D. Miracle, C. Chuang, and P. Liaw, Intermetallics **18**, 1758 (2010).
[3] O. Senkov, G. Wilks, J. Scott, and D. Miracle, Intermetallics **19**, 698 (2011).
[4] O. Senkov, J. Scott, S. Senkova, D. Miracle, and C. Woodward, J. Alloys Compd. **509**, 6043 (2011).
[5] H. Yao, J.-W. Qiao, M. Gao, J. Hawk, S.-G. Ma, and H. Zhou, Entropy **18**, 189 (2016).
[6] H. Yao, J. Qiao, M. Gao, J. Hawk, S. Ma, H. Zhou, and Y. Zhang, Mater. Sci. Eng., A **674**, 203 (2016).
[7] H. Yao, J. Qiao, J. Hawk, H. Zhou, M. Chen, and M. Gao, J. Alloys Compd. **696**, 1139 (2017).
[8] F. R. N. Nabarro, Proc. Phys. Soc. **58**, 669 (1946).
[9] R. Fleischer, Acta Metall. **9**, 996 (1961).
[10] R. Labusch, Phys. Status Solidi B **41**, 659 (1970).
[11] I. Toda-Caraballo and P. E. J. Rivera-Díaz-del-Castillo, Acta Mater. **85**, 14 (2015).
[12] I. Toda-Caraballo, J. S. Wróbel, S. L. Dudarev, D. Nguyen-Manh, and P. E. J. Rivera-Díaz-del-Castillo, Acta Mater. **97**, 156 (2015).
[13] C. Varvenne, A. Luque, and W. A. Curtin, Acta Mater. **118**, 164 (2016). **119**, 242 (2016).
[14] C. Varvenne, G. Leyson, M. Ghazisaeidi, and W. Curtin, Acta Mater. **124**, 660 (2017).
[15] C. Varvenne and W. A. Curtin, Scr. Mater. **138**, 92 (2017).
[16] M. C. Gao, J.-W. Yeh, P. K. Liaw, and Y. Zhang, *High-entropy Alloys: Fundamentals and Applications* (Springer, New York, 2016).
[17] N. L. Okamoto, K. Yuge, K. Tanaka, H. Inui, and E. P. George, AIP Adv. **6**, 125008 (2016).
[18] H. Song, F. Tian, Q.-M. Hu, L. Vitos, Y. Wang, J. Shen, and N. Chen, Phys. Rev. Materials **1**, 023404 (2017).
[19] W. G. Nöhring and W. Curtin, Scr. Mater. **168**, 119 (2019).
[20] T. Fukushima, H. Katayama-Yoshida, K. Sato, M. Ogura, R. Zeller, and P. H. Dederichs, J. Phys. Soc. Jpn. **86**, 114704 (2017).
[21] S. S. Sohn, A. Kwiatkowski da Silva, Y. Ikeda, F. Körmann, W. Lu, W. S. Choi, B. Gault, D. Ponge, J. Neugebauer, and D. Raabe, Adv. Mater. **31**, 1807142 (2019).
[22] T. Egami, M. Ojha, O. Khorgolkhuu, D. M. Nicholson, and G. M. Stocks, JOM **67**, 2345 (2015).

[23] H. S. Oh, S. J. Kim, K. Odbadrakh, W. H. Ryu, K. N. Yoon, S. Mu, F. Körmann, Y. Ikeda, C. C. Tasan, D. Raabe, T. Egami, and E. S. Park, Nat. Commun. **10**, 2090 (2019).

[24] R. F. W. Bader, *Atoms in Molecules: A Quantum Theory (International Series of Monographs on Chemistry)* (Clarendon Press, Oxford, 1994).

[25] H. Wang, M. Kohyama, S. Tanaka, and Y. Shiihara, J. Phys.: Condens. Matter **25**, 305006 (2013).

[26] L. V. Torne and G. Thomas, Acta Metall. **14**, 621 (1966).

[27] W. Guo, W. Dmowski, J.-Y. Noh, P. Rack, P. K. Liaw, and T. Egami, Metall. Mater. Trans. A **44**, 1994 (2013).

[28] C.-C. Juan, M.-H. Tsai, C.-W. Tsai, C.-M. Lin, W.-R. Wang, C.-C. Yang, S.-K. Chen, S.-J. Lin, and J.-W. Yeh, Intermetallics **62**, 76 (2015).

[29] A. Zunger, S.-H. Wei, L. G. Ferreira, and J. E. Bernard, Phys. Rev. Lett. **65**, 353 (1990).

[30] S. K. Bhattacharya, S. Tanaka, Y. Shiihara, and M. Kohyama, J. Phys.: Condens. Matter **25**, 135004 (2013).

[31] S. K. Bhattacharya, S. Tanaka, Y. Shiihara, and M. Kohyama, J. Mater. Sci. **49**, 3980 (2014).

[32] S. K. Bhattacharya, M. Kohyama, S. Tanaka, and Y. Shiihara, J. Phys.: Condens. Matter **26**, 355005 (2014).

[33] H. Wang, M. Kohyama, S. Tanaka, and Y. Shiihara, J. Mater. Sci. **50**, 6864 (2015).

[34] H. Wang, M. Kohyama, S. Tanaka, and Y. Shiihara, Modell. Simul. Mater. Sci. Eng. **25**, 015005 (2016).

[35] H. Wang, M. Kohyama, S. Tanaka, J. Wang, and Y. Chen, J. Phys.: Condens. Matter **31**, 095001 (2019).

[36] Z. Xu, S. Tanaka, and M. Kohyama, J. Phys.: Condens. Matter **31**, 115001 (2019).

[37] Y. Shiihara, M. Kohyama, and S. Ishibashi, Phys. Rev. B **81**, 075441 (2010).

[38] Y. Shiihara, M. Kohyama, and S. Ishibashi, Phys. Rev. B **87**, 125430 (2013).

[39] Y. Shiihara and M. Kohyama, Surf. Sci. **644**, 122 (2016).

[40] S. Ishibashi, T. Tamura, S. Tanaka, M. Kohyama, and K. Terakura, Phys. Rev. B **76**, 153310 (2007).

[41] K. Ichikawa and A. Tachibana, Phys. Rev. A **80**, 062507 (2009).

[42] K. Ichikawa, A. Wagatsuma, M. Kusumoto, and A. Tachibana, J. Mol. Struct. THEOCHEM **951**, 49 (2010).

[43] H. Nozaki, Y. Ikeda, K. Ichikawa, and A. Tachibana, J. Comput. Chem. **36**, 1240 (2015).

[44] K. Ichikawa, Y. Ikeda, A. Wagatsuma, K. Watanabe, P. Szarek, and A. Tachibana, Int. J. Quantum Chem. **111**, 3548 (2011).

[45] K. Ichikawa, A. Wagatsuma, P. Szarek, C. Zhou, H. Cheng, and A. Tachibana, Theor. Chem. Acc. **130**, 531 (2011).

[46] K. Ichikawa, H. Nozaki, N. Komazawa, and A. Tachibana, AIP Adv. **2**, 042195 (2012).

[47] K. Ichikawa, A. Wagatsuma, Y. I. Kurokawa, S. Sakaki, and A. Tachibana, Theor. Chem. Acc. **130**, 237 (2011).

[48] H. Nozaki, Y. Fujii, K. Ichikawa, T. Watanabe, Y. Aihara, and A. Tachibana, J. Comput. Chem. **37**, 1924 (2016).

[49] S. K. Bhattacharya, M. Kohyama, S. Tanaka, Y. Shiihara, A. Saengdeejing, Y. Chen, and T. Mohri, Mater. Res. Express **4**, 116518 (2017).

[50] H. Nozaki, K. Ichikawa, and A. Tachibana, Int. J. Quantum Chem. **116**, 504 (2016).

[51] A. Filippetti and V. Fiorentini, Phys. Rev. B **61**, 8433 (2000).

[52] M. Yu and D. R. Trinkle, J. Chem. Phys. **134**, 064111 (2011).

[53] P. E. Blöchl, Phys. Rev. B **50**, 17953 (1994).

[54] J. P. Perdew, K. Burke, and M. Ernzerhof, Phys. Rev. Lett. **77**, 3865 (1996).

[55] C.-L. Fu and K.-M. Ho, Phys. Rev. B **28**, 5480 (1983).

[56] S. Guo, C. Ng, J. Lu, and C. T. Liu, J. Appl. Phys. **109**, 103505 (2011).

[57] R. Chen, G. Qin, H. Zheng, L. Wang, Y. Su, Y. Chiu, H. Ding, J. Guo, and H. Fu, Acta Mater. **144**, 129 (2018).

[58] W. Fang, R. Chang, P. Ji, X. Zhang, B. Liu, X. Qu, and F. Yin, Metals **8**, 369 (2018).

[59] X. Wu, Z. Li, Z. Rao, Y. Ikeda, B. Dutta, F. Körmann, J. Neugebauer, and D. Raabe, (unpublished).

[60] H. S. Oh, D. Ma, G. P. Leyson, B. Grabowski, E. S. Park, F. Körmann, and D. Raabe, Entropy **18**, 321 (2016).

[61] J. C. Slater, J. Chem. Phys. **41**, 3199 (1964).

[62] L. Pauling, J. Am. Chem. Soc. **69**, 542 (1947).

[63] L. Pauling, J. Am. Chem. Soc. **54**, 3570 (1932).

[64] L. C. Allen, J. Am. Chem. Soc. **111**, 9003 (1989).

[65] J. B. Mann, T. L. Meek, and L. C. Allen, J. Am. Chem. Soc. **122**, 2780 (2000).

[66] J. B. Mann, T. L. Meek, E. T. Knight, J. F. Capitani, and L. C. Allen, J. Am. Chem. Soc. **122**, 5132 (2000).

[67] Y. Ikeda, I. Tanaka, J. Neugebauer, and F. Körmann, Phys. Rev. Materials **3**, 113603 (2019).

[68] R. G. A. Veiga, M. Perez, C. S. Becquart, C. Domain, and S. Garruchet, Phys. Rev. B **82**, 054103 (2010).

[69] O. Waseda, R. G. Veiga, J. Morthomas, P. Chantrenne, C. S. Becquart, F. Ribeiro, A. Jelea, H. Goldenstein, and M. Perez, Scr. Mater. **129**, 16 (2017).

[70] M. Soleymani, M. Parsa, and H. Mirzadeh, Comput. Mater. Sci. **84**, 83 (2014).

[71] F. Yazdandoost and R. Mirzaeifar, J. Alloys Compd. **709**, 72 (2017).

[72] P. Souvatzis, O. Eriksson, M. I. Katsnelson, and S. P. Rudin, Phys. Rev. Lett. **100**, 095901 (2008).

[73] P. Souvatzis, O. Eriksson, M. Katsnelson, and S. Rudin, Comput. Mater. Sci. **44**, 888 (2009).

[74] D. Korbmacher, A. Glensk, A. I. Duff, M. W. Finnis, B. Grabowski, and J. Neugebauer, Phys. Rev. B **100**, 104110 (2019).

[75] D. Korbmacher, Ph.D. thesis, Ruhr-Universität Bochum, 2019.

[76] F. Körmann, Y. Ikeda, B. Grabowski, and M. H. F. Sluiter, npj Comput. Mater. **3**, 36 (2017).

[77] Y. Ikeda, B. Grabowski, and F. Körmann, Mater. Charact. **147**, 464 (2019).

[78] T. Smith, M. Hooshmand, B. Esser, F. Otto, D. McComb, E. George, M. Ghazisaeidi, and M. Mills, Acta Mater. **110**, 352 (2016).

[79] Y. Ikeda, F. Körmann, I. Tanaka, and J. Neugebauer, Entropy **20**, 655 (2018).

[80] S. Zhao, Y. Osetsky, G. M. Stocks, and Y. Zhang, npj Comput. Mater. **5**, 13 (2019).

[81] J. Ding, Q. Yu, M. Asta, and R. O. Ritchie, Proc. Natl. Acad. Sci. U.S.A. **115**, 8919 (2018).

[82] W. P. Huhn and M. Widom, JOM **65**, 1772 (2013).

[83] W. P. Huhn, Ph.D. thesis, Carnegie Mellon University, 2014.

[84] M. Widom, W. P. Huhn, S. Maiti, and W. Steurer, Metall. Mater. Trans. A **45**, 196 (2014).

[85] F. Körmann and M. H. Sluiter, Entropy **18**, 403 (2016).

[86] F. Körmann, A. V. Ruban, and M. H. Sluiter, Mater. Res. Lett. **5**, 35 (2017).
[87] I. Toda-Caraballo, J. S. Wróbel, D. Nguyen-Manh, P. Pérez, and P. E. J. Rivera-Díaz-del-Castillo, JOM **69**, 2137 (2017).
[88] W. Y. Wang, S. L. Shang, Y. Wang, F. Han, K. A. Darling, Y. Wu, X. Xie, O. N. Senkov, J. Li, X. D. Hui, K. A. Dahmen, P. K. Liaw, L. J. Kecskes, and Z.-K. Liu, npj Comput. Mater. **3**, 23 (2017).
[89] B. Feng and M. Widom, Mater. Chem. Phys. **210**, 309 (2018).
[90] C. G. Schön, T. Duong, Y. Wang, and R. Arróyave, Acta Mater. **148**, 263 (2018).
[91] P. Singh, A. V. Smirnov, and D. D. Johnson, Phys. Rev. Materials **2**, 055004 (2018).
[92] Y. Wang, M. Yan, Q. Zhu, W. Y. Wang, Y. Wu, X. Hui, R. Otis, S.-L. Shang, Z.-K. Liu, and L.-Q. Chen, Acta Mater. **143**, 88 (2018).
[93] T. Kostiuchenko, F. Körmann, J. Neugebauer, and A. Shapeev, npj Comput. Mater. **5**, 55 (2019).
[94] T. Hammerschmidt, B. Seiser, M. Ford, A. Ladines, S. Schreiber, N. Wang, J. Jenke, Y. Lysogorskiy, C. Teijeiro, M. Mrovec, M. Cak, E. Margine, D. Pettifor, and R. Drautz, Comput. Phys. Commun. **235**, 221 (2019).
[95] G. K. White, Physica B+C **149**, 255 (1988).
[96] G. Kresse, J. Non-Cryst. Solids **192–193**, 222 (1995).
[97] G. Kresse and J. Furthmüller, Comput. Mater. Sci. **6**, 15 (1996).
[98] G. Kresse and D. Joubert, Phys. Rev. B **59**, 1758 (1999).
[99] M. Methfessel and A. T. Paxton, Phys. Rev. B **40**, 3616 (1989).
[100] P. Vinet, J. H. Rose, J. Ferrante, and J. R. Smith, J. Phys.: Condens. Matter **1**, 1941 (1989).

Correction: The license statement contained an omission and has been fixed.